International Journal of Mechanical, Industrial and Aerospace Sciences
ISSN: 2517-9950
Vol:12, No:8, 2018

Aeroacoustics Investigations of Unsteady 3D Airfoil for Different Angle Using Computational Fluid Dynamics Software

Haydar Kepekçi, Baha Zafer, Hasan Rıza Güven

***Abstract*—**Noise disturbance is one of the major factors considered in the fast development of aircraft technology. This paper reviews the flow field, which is examined on the 2D NACA0015 and 3D NACA0012 blade profile using SST k-ω turbulence model to compute the unsteady flow field. We inserted the time-dependent flow area variables in Ffowcs-Williams and Hawkings (FW-H) equations as an input and Sound Pressure Level (SPL) values will be computed for different angles of attack (AoA) from the microphone which is positioned in the computational domain to investigate effect of augmentation of unsteady 2D and 3D airfoil region noise level. The computed results will be compared with experimental data which are available in the open literature. As results; one of the calculated Cp is slightly lower than the experimental value. This difference could be due to the higher Reynolds number of the experimental data. The ANSYS Fluent software was used in this study. Fluent includes well-validated physical modeling capabilities to deliver fast, accurate results across the widest range of CFD and multiphysics applications. This paper includes a study which is on external flow over an airfoil. The case of 2D NACA0015 has approximately 7 million elements and solves compressible fluid flow with heat transfer using the SST turbulence model. The other case of 3D NACA0012 has approximately 3 million elements.

***Keywords*—**Aeroacoustics, Ffowcs-Williams and Hawkings equations, SST k-ω turbulence model, Noise Disturbance, 3D Blade Profile, 2D Blade Profile.

I. Introduction

RECENTLY, the rise in oil prices, the rapid depletion of fossil fuel reserves, and the negative effects of fossil fuels and energy production on the environment have led countries to turn to renewable energy sources. Renewable energy sources are clean energy sources that do not create environmental pollution and are unlimited. On the other hand, the use of these sources, which are available in most places and are completely free, reduces countries' dependence on energy.

Wind energy is the most common use of today's renewable energy resources. It is the most economical of the existing renewables. The use of wind energy in the production of electricity is constantly increasing in the world. World leader China has the power of 148 000 MW wind energy. Also, the USA has 74 347 MW, Germany has 45 192 MW, India has 24 759 MW, Spain has 22 987 MW and the United Kingdom has 13 614 MW [1].

Wind turbines that are built to provide energy needs also have some negative aspects. One of them is having a high level of sound problem associated with the blades as they rotate. Because of this problem, wind turbine farms cannot be built in cities or close to residential areas. In addition to noise pollution disturb their living spaces, this negative phenomenon can damage the ecological balance by modifying the migratory route of seasonal birds and can be addressed by providing aeroacoustic solutions.

In wind turbines, the sound is produced in two forms, these are: mechanical noise and aerodynamic noise. Mechanical noise is caused by the gearbox and moving parts in the generator. Noise can be reduced by using technologies such as acoustical isolation. However, aerodynamic noise sources are more complex and are not easy to control.

Aeroacoustic sources classified as monopole, dipole, and quadrupole. Monopole and dipole resources; are welded near the surfaces and are strong emitters of acoustic energy. Quadrupole sources are welded away from the surfaces and are weak emitters. For example, a highly turbulent flow can be generated by the wind turbine. Aerodynamic noise caused by a wind turbine is due to the unstable flow at the surface of the turbine blade, which causes strong dipole sources.

Brooks and Schlinker developed two main aeroacoustic noise mechanisms to facilitate understanding of complex sources and apply models to the semi-empirical noise estimation code. The first mechanism is the swallowing noise, which is a function of swirl turbulence. The acoustical noise has shown that the low-frequency powers in the spectrum are mainly turbulent input sources [2].

The second noise mechanism is the one that produces the aerofoil, which is a function of the parametric geometry. The sound that the aerofillers produce can be divided into different subtitles. These subtitles are the rear edge of the turbulent boundary layers that can be divided into the noises of the rear edge, the separation and the stop noise, the rear edge blindness, and the swirl swing noise and the tip swirl noise.

As an alternative to empirical methods, Computational Flow Dynamics and Computational Aeroacoustic Methods are used. For accurate estimation of the formation of noise in a wind turbine, a well-solved transient flow field near the surface of the blade is required. Methods such as Direct Numerical Simulation (DNS) or Large Eddy Simulation (LES) can be used to calculate the irregular turbulence flow field.

Kepekçi H. is with the Mechanical Engineering Department, Beykent Universtiy, İstanbul, Turkey (e-mail: haydarkepekci@beykent.edu.tr).

Zafer B. and Güven H. R. are with the Mechanical Engineering Department, İstanbul University, İstanbul, Turkey (e-mail: baha.zafer@istanbul.edu.tr, hrguven@istanbul.edu.tr).

These methods include the need of high quality mesh particles around the airfoil surface. In order to avoid numerical instability when the fine mesh is used, it also requires high simulation requirements in the simulation. The LES solution is cheaper than DNS and gives acceptable results in aeroacoustic analysis [3].

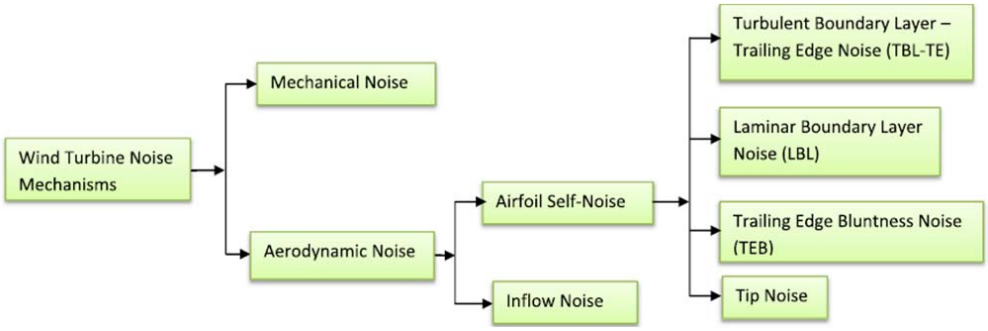

Fig. 1 Sound Generation in Wind Turbines

Migliore has prepared a study for aeroacoustic tests on the wind tunnels. The purpose of these tests is boundary layer effect on acoustical emissions, the effect of end zone form and effect of back edge thickness. These tests were applied under realistic conditions with 170,000 to 397,000 Reynolds numbers. During the tests, six end shapes, three border layer height, two rear edge thickness and 72 speed/attack angle points were used. In experiments with low speeds (Reynolds Number: 170,000), a 3.8 dB difference in total SPL was observed when the parameters were changed. However, in high-speed experiments (Reynolds Number: 315,000) this difference has been reduced to 1.3 dB. Based on these results; it was concluded that the wind turbine is an important factor in reducing the noises of the tip-shaped rotation in its wings [4].

Ghasemian and Nejat, H-Darrieus numerically predicted the aerodynamic noise emitted from the vertical axis wind turbine using the FW-H simulation formulation. The simulations performed in this process were performed for five different end-to-speed ratios. First, the average torque coefficient is compared with the experimental data and a good fit is observed. Then, in the study, they focused on the broadband sounds of the turbulent border layers and the tonal voices connected to the wing transition frequency. As a result, it is clear that there is a direct relationship between the emitted noise and the speed of rotation.

Also, the effect of receiver distance on the General SPL was investigated. They have seen a logarithmic change of the receiver distance with the General SPL [5].

Mohamed et al. studied low velocity wind speeds using Darrieus wind turbines and calculated the numerical model of rotor performance using ANSYS Workbench and tested different wing types to achieve the best performance. They found that the zero slope angle gives the best performance from the comparable wing angles. Also, they concluded that the analysis using SST k-ω is the most accurate [6].

In the study, symmetric NACA 0012 aerofoil was formed in the stationary domain. The appropriate mesh is prepared with the Pointwise program. It was simulated using ANSYS Fluent with the SST k-ω method. In total, eight microphones, four in the leading edge section and four in the trailing edge section, were placed on the airfoil. Numerical values of acoustic data were obtained from these microphones and acoustic analogy calculated using the simulation program, ANSYS Fluent. The values obtained from eight microphones were compared, and the results showed the regions where the highest levels of disturbance are found.

II. Numerical Method

Numerical discretization of time-dependent constitutive equations for the flow field was performed with the ANSYS Fluent commercial computational fluid dynamics solver. In this study, closed-time schemes were used to facilitate the unit frequency step to be used in acoustical solutions, while the finite volume approach, which provides protection principles for the unit volume, is used in discretizing the variables in the flow field [7].

A second-order upwind scheme is used for both spatial and temporal discretization. Conservation equations for the flow field are given in (1) in the integral form [8].

$$\frac{\partial}{\partial t}\int_v WdV + \oint (F-G).dA = \int_v HdV \quad (1)$$

The flow solution vector W, the convective flux matrix F, and the viscous flux matrix G are expressed in Equation 2;

$$W=\begin{Bmatrix}\rho\\ \rho u\\ \rho v\\ \rho w\\ \rho E\end{Bmatrix}, F=\begin{Bmatrix}\rho V\\ \rho Vu+pi\\ \rho Vv+pj\\ \rho Vw+pk\\ V(\rho E+p)\end{Bmatrix}, G=\begin{Bmatrix}0\\ \tau_{xi}\\ \tau_{yi}\\ \tau_{zi}\\ \tau_{ij}v_j+q\end{Bmatrix}, H=\begin{Bmatrix}0\\ f_x\\ f_y\\ f_z\\ \rho(f_i v_j \delta_{ij})+\dot{q}_h\end{Bmatrix} \quad (2)$$

where, ρ = density of fluid, v = ui + vj + wk velocity vector, V is the speed of contravariant definition, V = v.n and n surfaces are defined as normal. E is the total energy in mass, p is the pressure, τ_{ij} is the viscous tension tensor, and τ is the heat flux. In the H source term, the volume effect forces (gravity, Cornelius acceleration, etc.) and qh term indicate the time dependent heat source produced in the volume. For low Mach

number flows, the difficulty in solving the momentum equation arises due to the fact that the time-dependent term in the continuity relation decreases as the density is constant. In the numerical form of Navier-Stokes equations, this problem is eliminated by preconditioning. The derivative term according to the time is multiplied by the preconditioning matrix. Thus, the constituent relations used for the solution in (3) are expressed in the most general way [9].

$$\frac{\partial W}{\partial Q}\frac{\partial}{\partial t}\int_V QdV + \oint (F-G).dA = \int_V HdV \quad (3)$$

The Q solution vector is rewritten according to the primary variables defined in (4) and is given in below

$$Q = \begin{Bmatrix} p \\ u \\ v \\ w \\ T \end{Bmatrix}, \frac{\partial W}{\partial Q} = \begin{bmatrix} \rho_p & 0 & 0 & 0 & \rho_T \\ \rho_p u & \rho & 0 & 0 & \rho_T u \\ \rho_p v & 0 & \rho & 0 & \rho_T v \\ \rho_p w & 0 & 0 & \rho & \rho_T w \\ \rho_p H - \delta & \rho u & \rho v & \rho w & \rho_T H + \rho C_p \end{bmatrix} \quad (4)$$

when $\rho_p = \partial\rho/\partial p$, $\rho_T = \partial\rho/\partial T$ is defined, ρ = 0 is taken for incompressible flow. Thus, the decompression scheme used in the incompressible flow domain solutions is obtained [7]. In (1) and (2), according to the Boussinesq approach; τ_{ij} is the Reynolds stress-strain, expressed as (5) below [9].

$$\tau_{ij} = -\rho\overline{u'_i u'_j} = \mu_t\left(\frac{\partial u_i}{\partial x_j} + \frac{\partial u_j}{\partial x_i}\right) - \frac{2}{3}\delta_{ij}\rho k \quad (5)$$

where u'_i and u'_j are turbulence velocity fluctuations, μt is the turbulence viscosity, δij is the Kronecker Delta. Since the SST k–ω model provides high success in external flow calculations, this turbulence model was used in this study.

A. FW-H Acoustic Analogy

Ffowcs William and Hawkings utilized the generalized function theory to obtain the classic equation associated with their names. The FW-H equation can be written as the following nonuniform wave equation

$$\frac{1}{c}\frac{\partial^2 p'(x,t)}{\partial t^2} - \nabla^2 p'(x,t) = \frac{\partial}{\partial t}\left[(\rho_0 U_n)\delta(f)\right] - \frac{\partial}{\partial x_i}[L_i\delta(f)] + \frac{\partial^2}{\partial x_i \partial x_j}\left[T_{ij}H(f)\right] \quad (6)$$

where the three terms on the right-hand side are the monopole, dipole, and quadrupole sources, respectively (from left to right).

$$U_i = \left(1 - \frac{\rho}{\rho_0}\right)v_i + \frac{\rho u_i}{\rho_0} \quad (7)$$

$$L_i = \left[(p-p_0)\delta_{ij} - \tau_{ij} + \rho u_i(u_j - v_j)\right]n_j \, . \quad (8)$$

$$T_{ij} = \rho u_i u_j + [(p-p_0) - c^2(\rho-\rho_0)]\delta_{ij} - \tau_{ij} \quad (9)$$

where p' is the far field pressure fluctuations, T_{ij} is the Lighthill stress tensor, $\delta(f)$ is the Dirac delta function, ρ_0 is the ambient density, p_0 is the ambient pressure, H is the Heaviside function, u is the fluid velocity, v is the body surface velocity, c is the velocity of sound, n is a normal vector that points into the fluid [10].

The far field solution of the FW-H equation can be written as:

$$4\pi p'_T(x,t) = \int_{f=0}\left[\frac{\rho_0(\dot{U}_n + U_n)}{r(1-M_r)^2}\right]_2 dS + \int_{f=0}\left\{\frac{\rho_0 U_n[r\dot{M}_r + c(M_r - M^2)]}{r^2(1-M_r)^3}\right\}_{ret} dS \quad (10)$$

where M is the Mach number vector at a source point on the integration surface, dots on quantities denote time derivative with respect to the source time τ, and the remaining terms are defined as

$$U_n = U_i\hat{n}_i$$
$$U_{\dot{n}} = U_i\hat{n}_i$$
$$\dot{U}_n = \dot{U}_i\hat{n}_i$$
$$M_r = M_i\hat{r}_i$$
$$\dot{M}_r = \dot{M}_i\hat{r}_i$$

$$4\pi p'_L(x,t) = \frac{1}{c}\int_{f=0}\left[\frac{\dot{L}_r}{r(1-M_r)^2)}\right]_{ret} dS + \int_{f=0}\left[\frac{L_r - L_M}{r^2(1-M_r)^2}\right]_{ret} dS + \frac{1}{c}\int_{f=0}\left\{\frac{L_r[r\dot{M}_r + c(M_r - M^2)]}{r^2(1-M_r)^3}\right\}_{ret} dS. \quad (11)$$

where

$$L_r = L_i\hat{r}_i$$
$$\dot{L}_r = \dot{L}_i + \hat{r}_i$$
$$L_m = L_i M_i$$
$$4\pi p'_Q(x,t) = \int_{f>0}\left[\frac{K_1}{c^2 r} + \frac{K_2}{cr^2} + \frac{K_3}{r^2}\right]dV \, . \quad (12)$$

$$K_1 = \frac{\ddot{T}_{rr}}{(1-M_r)^3} + \frac{\ddot{M}_r T_{rr} + 3\dot{M}_r\dot{T}_{rr}}{(1-M_r)^4} + \frac{3\dot{M}_r{}^2 T_{rr}}{(1-M_r)^5}. \quad (13)$$

$$K_2 = \frac{-\ddot{T}_{ii}}{(1-M_r)^2} - \frac{4\dot{T}_{Mr} + 2T_{\dot{M}r} + \dot{M}_r T_{ii}}{(1-M_r)^3} + \frac{3\left[(1-M^2)\dot{T}_{rr} - 2\dot{M}_r T_{Mr} - M_i\dot{M}_i T_{rr}\right]}{(1-M_r)^4} + \frac{6\dot{M}_r(1-M^2)T_{rr}}{(1-M_r)^5} \quad (14)$$

$$K_3 = \frac{2T_{MM} - (1-M^2)T_{ii}}{(1-M_r)^3} - \frac{6(1-M^2)T_{M_r}}{(1-M_r)^4} + \frac{3(1-M^2)^2 T_{rr}}{(1-M_r)^5} \quad (15)$$

where $T_{rr} = T_{ij}\hat{r}_i\hat{r}_j$ is the double contraction of the Lighthill stress tensor T_{ij} , and the other terms are defined as:

$$T_{MM} = T_{ij}M_iM_j \, , T_{M_r} = T_{ij}M_i\hat{r}_j \, , T_{\dot{M}_r} = T_{ij}\dot{M}_i\hat{r}_j \, ,$$
$$\dot{T}_{M_r} = \dot{T}_{ij}M_i\hat{r}_j \, , \dot{T}_{rr} = \dot{T}_{ij}\hat{r}_i\hat{r}_j \, , \ddot{T}_{rr} = \ddot{T}_{ij}\hat{r}_i\hat{r}_j \, ,$$

where M is the Mach number vector of a volume source fixed in the body reference frame. Some comprehensive definition could be found [11].

The SPL is calculated in decibels using the RMS magnitudes at the relevant time interval of the time-dependent pressure values.

$$SPL = 20\log\left(\frac{p'_{rms}}{p_{ref}}\right) \text{ and } p_{ref} = 2x10^{-05}\ Pa$$

B. SST k-ω Governing Equations

The SST k-ω turbulence model is a two-equation eddy-viscosity model which has become very popular. The shear stress transport (SST) formulation combines the best of two worlds. The use of a k-ω formulation in the internal parts of the boundary layer makes the model straight usable all the way down to the wall through the viscous sub-layer, hereby the SST k-ω model can be used as a Low-Re turbulence model without any additional damping functions [12].

The SST formulation further switches to a k-ε attitude in the free-stream and by that means avoids the widespread k-ω problem that the model is so sensitive to the inlet free-stream turbulence properties. Authors who use the SST k-ω model often merit it for its good behavior in adverse pressure gradients and separating flow.

The SST k-ω model does produce a bit too large turbulence levels in regions with large normal strain, like stagnation regions and regions with strong speed-up. This propensity is many less marked than with a normal k-ε model though [13].

Turbulence Kinetic Energy is:

$$\frac{\partial k}{\partial t} + U_j\frac{\partial k}{\partial x_j} = P_k - \beta * k\omega + \frac{\partial}{\partial x_j}\left[(v + \sigma_k v_T)\frac{\partial k}{\partial x_j}\right] \quad (16)$$

Specific Dissipation Rate calculated as:

$$\frac{\partial \omega}{\partial t} + U_j\frac{\partial \omega}{\partial x_j} = \alpha S^2 - \beta\omega^2 + \frac{\partial}{\partial x_j}\left[(v + \sigma_\omega v_T)\frac{\partial \omega}{\partial x_j}\right] + 2(1 - F_1)\sigma_{\omega^2}\frac{1}{\omega}\frac{\partial k}{\partial x_i}\frac{\partial \omega}{\partial x_i} \quad (17)$$

Closure Coefficients and Auxiliary Relations

F_2 (second blending function) is calculated as:

$$F_2 = tanh\left[\left[\max\left(\frac{2\sqrt{k}}{\beta * \omega y}, \frac{500v}{y^2\omega}\right)\right]^2\right] \quad (18)$$

P_k (Production limiter) is defined:

$$P_k = \min\left(\tau_{ij}\frac{\partial U_i}{\partial x_j}, 10\beta * k\omega\right) \quad (19)$$

Each of the constants is a blend of an inner (1) and outer (2) constant, blended via:

$$\emptyset = \emptyset_1 F_1 + \emptyset_2(1 - F_1) \quad (20)$$

where $\emptyset_1$ represents constant 1 and $\emptyset_2$ represents constant 2.

Additional functions are given by:

F_1 (Blending Function) is calculated as:

$$F_1 = tanh\left\{\left\{min\left[\max\left(\frac{\sqrt{k}}{\beta * \omega y}, \frac{500v}{y^2\omega}\right), \frac{4\sigma_{\omega^2}}{CD_{k\omega}y^2}\right]\right\}^4\right\} \quad (21)$$

Note: F_1=1 inside the boundary layer and 0 in the free stream.,

$$CD_{k\omega} = \max(2\rho\sigma_{\omega 2}\frac{1}{\omega}\frac{\partial k}{\partial x_i}\frac{\partial \omega}{\partial x_i}, 10^{-10}) \quad (22)$$

And ρ is the density, $v_t = {\mu_t}/{\rho}$ is the turbulent kinematic viscosity, μ is the molecular dynamic viscosity, and y is the distance from the field point to the nearest wall [14].

Kinematic eddy viscosity is defined as:

$$v_T = \frac{\alpha_1 k}{\max(\alpha_1\omega, SF_2)} \quad (23)$$

The boundary conditions recommended in the original reference are:

$$\frac{U_\infty}{L} < \omega_{far\ field} < 10\frac{U_\infty}{L}. \quad (24)$$

$$\frac{10^{-5}U^2_\infty}{R_{eL}} < k_{far\ field} < \frac{0.1U^2_\infty}{R_{eL}}. \quad (25)$$

$$\omega_{wall} = 10\frac{6v}{\beta_1(\Delta d_1)^2}. \quad (26)$$

$$k_{wall} = 0$$

where L is the approximate length of the computational domain, and the combination of the two far-field values should yield a free stream turbulent viscosity between 10^{-5} and 10^{-2} times free stream laminar viscosity. Thus, the far-field turbulence boundary conditions are somewhat open to interpretation. Note that the turbulence variables decay (sometimes dramatically) from their set values in the far-field for external aerodynamic problems.

The constants are:

$$\alpha_1 = \frac{5}{9}, \alpha_2 = 0.44$$
$$\beta_1 = \frac{3}{40}, \beta_2 = 0.0828$$
$$\beta^* = \frac{9}{100}$$
$$\sigma_{k1} = 0.85, \sigma_{k2} = 1$$
$$\sigma_{\omega 1} = 0.5, \sigma_{\omega 2} = 0.856$$

III. Aerofoil Confirmation

A. Mesh Generation

The aeroacoustic simulation methodology was tested on NACA series aerofoils which were created using Pointwise. After the calculations are finished, the results of 3D NACA0012 are compared with data from Brooks et al. [15] and the results of 2D NACA0012 are compared with data from the work of Zhang et al. (2016) [18].

The NACA series are aerofoils developed by the National Advisory Committee for Aeronautics and have been extensively used in the aerospace industry for research owing to their simple geometric design.

The mesh image of the airfoils studied is as shown in Fig. 2. Also, the 3D mesh domain prepared is shown in Fig. 3. The NACA0015 chord length used in C=0.61 m and span of 1.8 m. This mesh has contained about 7 million cells.

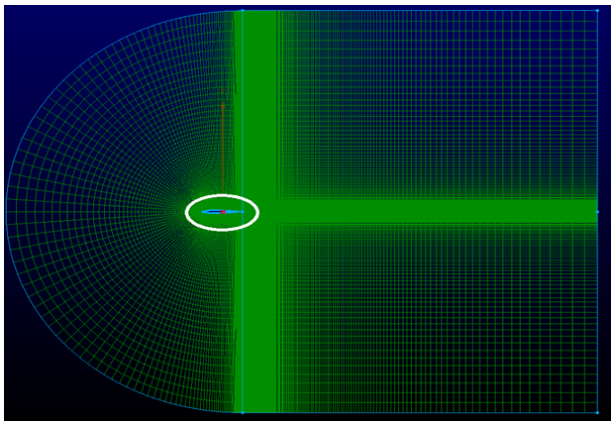

Fig. 2 General view of meshes prepared using Pointwise

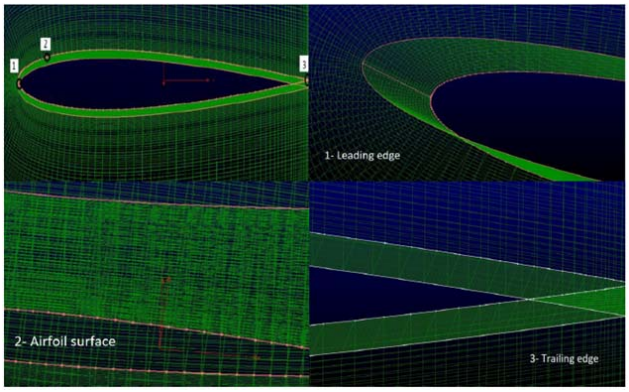

Fig. 3 Zoom of different zones where the 3D NACA0012 mesh that simulating

The NACA 0012 aerofoil chord length used in C=0.3048 m to equal the experimental data. The span used is 0.1143 m that are 1/4 of the experimental span (S) used by Brooks et al. [15]. The distance from the main inlet boundary to the leading edge of the blade is 6C and the distance from the leading edge to the main outlet boundary is 12C. This mesh has contained about 3 million cells. The geometry of the aerofoils and their mesh was created using Pointwise. The meshes are structured near the blade and unstructured in the far field.

Velocity inlet and pressure outlet limits are used to simulate distance field locations.

For inlet boundaries, it was selected that free stream velocity is 71.3 m/s and Reynolds.

Number is $1.5x10^6$ for NACA0012. Also, NACA0015 aerofoil's free stream velocity is 30 m/s and Reynolds Number is $1.3x10^6$. The velocity value changes according to the airfoil's AoA. This change is calculated according to the following formula where is $u = U_\infty cos(\alpha)$, $v = U_\infty sin(\alpha)$ and $w = 0$, and U_∞ is the free stream velocity and α is the AoA.

A steady-state RANS (Reynolds Averaged Navier Stokes) solution was developed to create a steady state before starting the SST k-ω solution. This process lasted 0.05 s. The convergence criterion is 10^{-6} for all residuals. The SIMPLE algorithm (Semi-Implicit Method for Pressure-Linked Equations) was used for the SST k-ω method solved using a second-order central differencing scheme. A time step size of 10^{-5} sn was selected. The simulation stabilized in 0.3 s. It was stopped at 0.35 s and the results were checked.

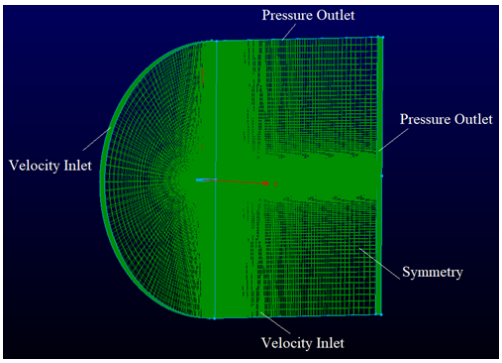

Fig. 4 Rectangular Domain for NACA 0012 for showing the boundary conditions

C. CFD Results

To confirm the simulations, the coefficients of pressure and lift were compared with experimental data. These comparisons are given in the graphs below. The lift coefficient value is calculated as:

$$c_L = \frac{L}{\frac{1}{2}\rho_\infty {U_\infty}^2 S}. \quad (27)$$

In this equation, L represents the total lift force and ρ_∞ represents the free stream fluid density.

The pressure coefficients value is calculated as:

$$c_p = \frac{p - p_\infty}{\frac{1}{2}p_\infty {U_\infty}^2}. \quad (28)$$

p_∞ represents ambient pressure.

For 3D NACA0012, two different AoA values as 0° and 5.4° were used in this study. The time-averaged lift coefficient has been appraised for SST k-ω calculations at two different AoA and is shown in Fig. 5. When the experimental data of Abbott and Von-Doenhoff [17] are compared, similar results were obtained for the calculation made for 0°; numerical differences have been found in calculations made for 5.4°.

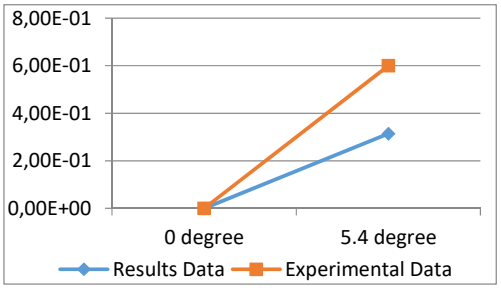

Fig. 5 c_L SST- kω method results of 3D NACA0012 aerofoil compared with experimental data of Abbott and Von-Doenhoff's paper [17]

In Figs. 6 and 7, the time-averaged pressure coefficient data acquired using SST k-ω calculations compared with experimental data by Gregory and O'Reilly [16]. In the analyses made, the cp value obtained for 0° is close to the experimental data. But the cp value obtained from the calculations made for 5.4° is lower than the experimental data. This difference may be due to the lack of a more precise study using the LES method.

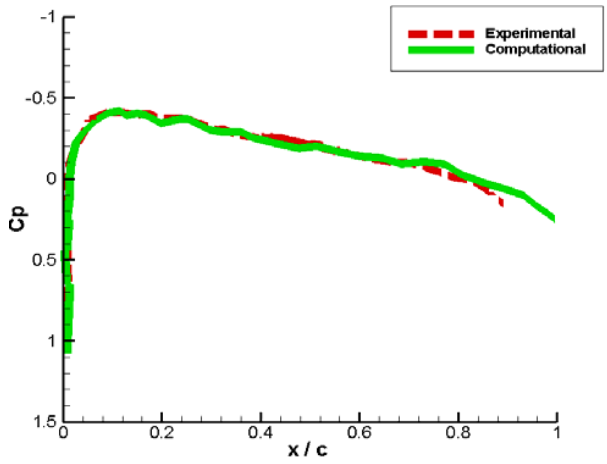

Fig. 6 SST k-ω results of the pressure coefficient for the 3D NACA0012 at 0°

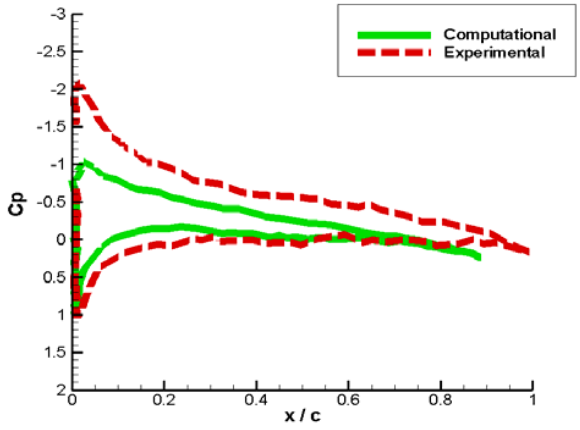

Fig. 7 SST k-ω results of the pressure coefficient for the 3D NACA0012 at 5.4°

In Figs. 8 and 9, the time-averaged pressure coefficient data acquired using SST k-ω calculations compared with experimental data from the work of Zhang et al. (2016). In the analyses made, the cp value obtained both 0° and 8° is close to the experimental data.

D. Acoustic Results

A total of eight receivers were used in the analysis for 3D NACA0012. Four of these acoustic receivers were placed in the front of the airfoil and the other four on the back. In the acoustic analysis for 2D NACA0015, only one receiver was used and placed on the back of the airfoil.

The results obtained from the receivers returned online when the steady-state analysis is initiated are compared with the experimental data. The data from the recipients were based on those closest to the experimental results. Detailed numerical results can be seen in the following figures.

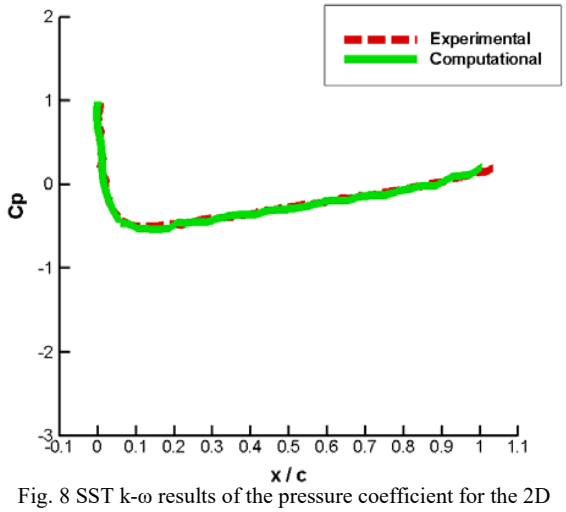

Fig. 8 SST k-ω results of the pressure coefficient for the 2D NACA0015 at 0°

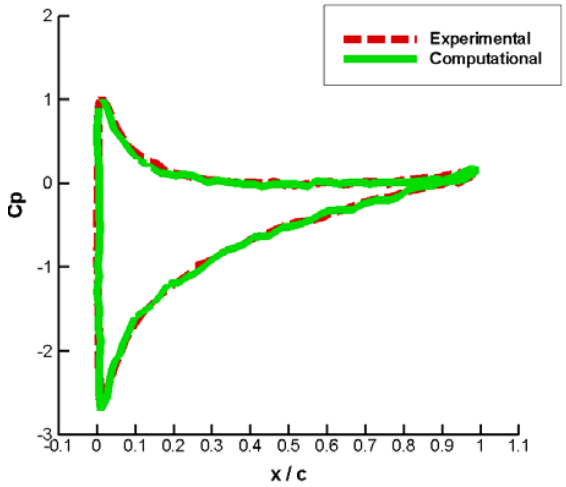

Fig. 9 SST k-ω results of the pressure coefficient for the 2D NACA0015 at 8°

In all of the analyses performed, the calculated SPL values were lower than the experimental data. This may be due to the fact that the turbulence zone has not been fully formed and that the calculations have not been done by the LES method.

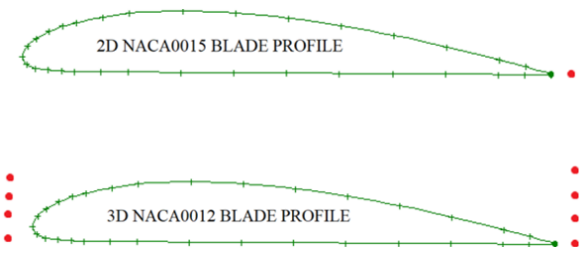

Fig. 10 Microphone positions on the prepared airfoils mesh

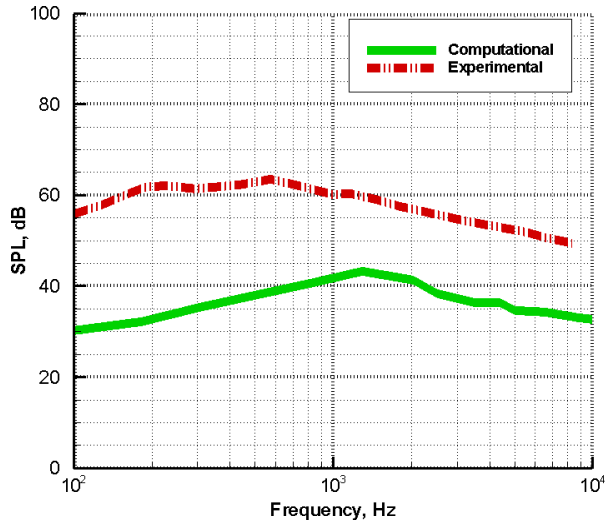

Fig. 11 Acoustic results for the 3D NACA0012 at 0°

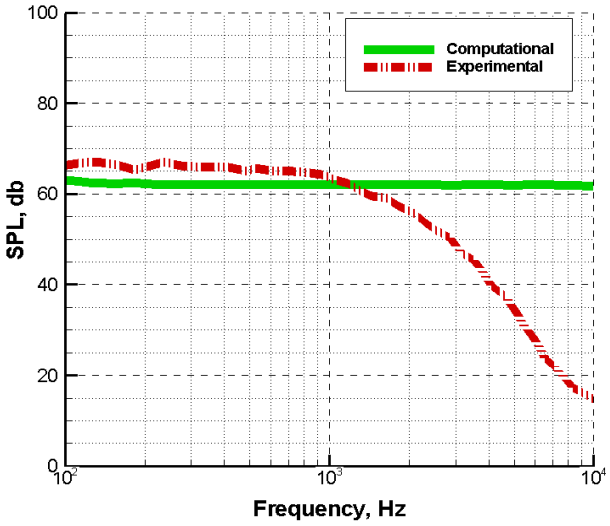

Fig. 12 Acoustic results for the 2D NACA0015 at 0°

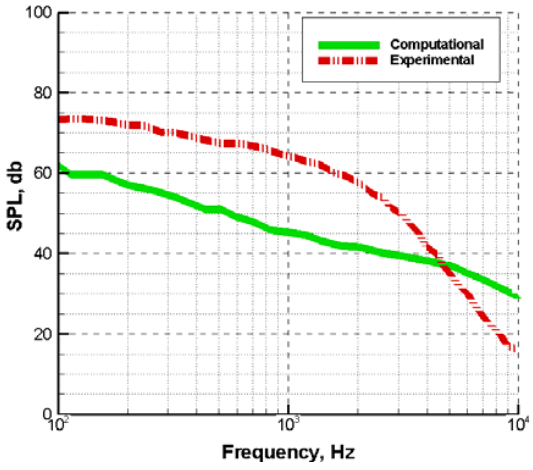

Fig. 13 Acoustic results for the 2D NACA0015 at 8°

IV. Conclusions

The forecast of the based on the wind noise is a significant and complicated problem in the fluid-dynamic acoustics area. Recently, some acoustic methods in CFD are developed for the acoustic area forecast. In the analysis, acoustic estimates were made using the SST k-ω model. When the studies in the literature are examined, it is seen that this method is widely used. However, in the analyzes made, the number of Reynolds is higher than the examined articles and the end result of the calculations of the turbulent zone accounts is not the desired result, although the cp diagrams were taken properly, errors were found in the SPL graphs. It is clear that this area needs more work. In the following periods, the flow-based sound can be completely estimated by the fact that the simulation programs continue to develop. In order to compare the numerical data to be obtained from the analyses to be made, it is necessary to develop it in experimental data. There are many other issues to work on in this field.

References

[1] (WWEA, 2016); http://www.wwindea.org/the-world-sets-new-wind-installations-record-637-gw-new-capacity-in-2015/.
[2] Brooks T., Schlinker R.; Progress in rotor broadband noise research; Vertica 7; 1983; 287–307.
[3] Wasala S., Storey R., Norris S., Cater J.; Aeroacoustic noise prediction for wind turbines using Large Eddy Simulation; Journal of Wind Engineering and Industrial Aerodynamics; 2015; 17-28.
[4] Migliore P; The potential for reducing blade-tip acoustic emissions for small wind turbines. Subcontractor Report; NREL/SR-500-43472; 2009; 4.
[5] Ghasemian M., Nejat A.; Aero-acoustics prediction of a vertical axis wind turbine using Large Eddy Simulation and acoustic analogy; Energy 2015; 711-717.
[6] Mohamed H. H., Ali A. M., Hafiz A. A.; CFD analysis Journal for H-rotor Darrieus turbine as a low speed wind energy converter; Engineering Science and Technology; 2015; 1-13.
[7] Laiping Z., Ming L., Wei L., Xin H., An implicit algorithm for high-order DG/FV schemes for compressible flows on 2D arbitrary grids, Communications in Computational Physics, 17 (1), 287-316, 2015.
[8] FLUENT Theory Guide14.0, 2013.
[9] Zafer B., Coşgun F., Zamana Bağlı Sıkıştırılamaz Kavite Akışının Aeroakustik Analizi, Journal of the Faculty of Engineering and Architecture of Gazi University 31:3, 2016, 665-675.
[10] Hang N., Xıe H., Wang X., Wu B., Computation of Vortical Flow and Flow Induced Noise by Large Eddy Simulation with FW-H Acoustic Analogy and Powell Vortex Sound Theory, Journal of Hydrodynamics, 2016, 28(2):255-266.
[11] Di Francescantonio P., A New Boundary Integral Formulation for the Prediction of Sound Radiation, Journal of Sound and Vibration, 1997, 202(4): 491-509.
[12] Hang N., Research on Mechanism and Hybrid Computation Approach for Cavity Flow and Flow Induced Noise, Doctoral Thesis, Wuxi, China: China Ship Scientific Research Center, 2010.
[13] Menter, F. R., "Zonal Two Equation k-ω Turbulence Models for Aerodynamic Flows", AIAA Paper 93-2906, 1993.
[14] Menter, F. R., "Two-Equation Eddy-Viscosity Turbulence Models for Engineering Applications", AIAA Journal, vol. 32, no 8. pp. 1598-1605, 1994.
[15] Brooks, T. F., Pope, D. S., Marcolini, M. A, 1989. Airfoil Self-Noise and Prediction. NASA RP 1218.
[16] Gregory, N., O'Reilly, C. L., 1973. Low-Speed Aerodynamic Characteristics of NACA0012 Aerofoil Section, Including the Effects of Upper-Surface Roughness Simulating Hoar Frost. Aeronautical Research Council Reports and memoranda. 3726.
[17] Abbott, I. H., Von-Doenhoff, A. E., 1959. Theory of Winging Sections, ıncluding a Summary of Airfoil Data, Dover Publications, Mineola, NY, USA.
[18] Zhang N., Xie H., Wang X., Wu B., Computation of vortical flow and

flow induced noise by large eddy simulation with FW-H acoustic analogy and Powell vortex sound theory, Journal of Hydrodynamics, 2016, 28(2):255-266.